ELSEVIER

Comput. Methods Appl. Mech. Engrg. 190 (2001) 2207–2226

Computer methods in applied mechanics and engineering

www.elsevier.com/locate/cma

Constitutive modeling of viscoelastic materials with damage – computational aspects

Marcelo E. Canga [a,*], Eric B. Becker [b], Şebnem Özüpek [b]

[a] *Ultramarine, 3100 South Gessner, Suite 325, Houston, TX 77063, USA*

[b] *Department of Aerospace Engineering and Engineering Mechanics, University of Texas at Austin, Austin, TX 78712, USA*

Received 2 July 1999

Abstract

The finite element implementation of a constitutive model for viscoelastic materials with damage is presented. The material model, originally developed in [Ş. Özüpek, E.B. Becker, Constitutive equations for solid propellants, J. Engrg. Matls. Tech. 199 (1997) 125–132] has been modified to allow an efficient numerical implementation in a finite element code. A step-by-step discussion of the calibration of the material coefficients is provided, including the calibrations of the damage and cyclic loading functions. The new formulation is illustrated with representative examples for pressurization of a solid propellant rocket motor. © 2001 Elsevier Science B.V. All rights reserved.

1. Introduction

Among the many industrial applications which involve nonlinear viscoelastic materials, we are interested in solid rocket propellants. These materials are particulate composites with a lightly cross-linked elastomeric binder that is filled with a high level of energetic constituents. Dewetting of the particles, temperature effects, and a large range of deformations result in a highly nonlinear response of the material.

The motivations in formulating the model and its development were originally discussed in [1]. In this paper, the main objective is to present the computational implementation of the model using the finite element method. We also present numerical algorithms for the calibration of the model using a small amount of experimental data. Representative examples are shown to illustrate the effectiveness of the model and its computational implementation.

The model is based on a phenomenological approach. The main characteristics of the model are:

- It is applicable to large deformations and rotations.
- It employs a dilatation model which represents the formation and growth of voids at or near the binder–particle interface. The effects of distortion and superimposed pressure on volume change are incorporated through this model.
- The model represents softening due to damage and accounts for nonlinearities during cyclic loading. Both phenomena are formulated through the use of internal state variables.
- Calibration procedures require data from only a small number of relatively easy tests.

* Corresponding author. Tel.: +1-713-975-8146; fax: +1-713-532-5450.

E-mail addresses: marcelo@ultramarine.com (M.E. Canga), becker@orion.ae.utexas.edu (E.B. Becker), sebnem@ticam.utexas.edu (S. Özüpek).

0045-7825/01/$ - see front matter © 2001 Elsevier Science B.V. All rights reserved.
PII: S0045-7825(00)00231-0

In Section 2, we describe the governing equations. In Section 3, we outline the numerical algorithm used in the finite element implementation. In Section 4, we discuss the material model calibration. In Section 5, we present some numerical examples from solid rocket motor analyses and compare finite element predictions with the test data.

2. Viscoelastic model. Mathematical formulation

In this section, we present the mathematical formulation of the viscoelastic model. As a preliminary, we discuss the elastic response of the material, which can be interpreted as the viscoelastic response for slow-varying processes. Since the primary application of this formulation is for materials that can be characterized as nearly incompressible, the well-known 'locking' computational problem is avoided by using a three-field variational formulation [2]. In this formulation the dilatation is treated as an independent variable. The dilatation is then constrained to the determinant of the deformation gradient using a Lagrange multiplier technique. The rheologic aspect of the viscoelastic material is subsequently introduced using hereditary integrals on the elastic stresses.

2.1. Elastic response

The elastic response of the material model is based on a strain energy density function. The energy function is chosen as an additive decomposition of energy due to distortional and dilatational deformation. Since the dilatation is treated as an independent variable, an extra term that ties it to the determinant of the deformation gradient through a Lagrange multiplier is added

$$\phi(\bar{I}_1, \bar{I}_2, \theta, s_i, c, T) = g(s_1) f(s_2, s_3) \bar{\phi}(\bar{I}_1, \bar{I}_2) + \hat{\phi}(\theta, c, T) + \lambda(J - \theta). \tag{1}$$

where ϕ is the elastic strain density energy, $\bar{\phi}$ the distortional part of the strain energy density, $\hat{\phi}$ the dilatational part of the strain energy density, $\mathrm{tr}(\cdot)$ the trace operator, $\bar{I}_1 = \mathrm{tr}\,\bar{\mathbf{C}}$, $\bar{I}_2 = \frac{1}{2}[(\mathrm{tr}\,\bar{\mathbf{C}})^2 - \mathrm{tr}\,\bar{\mathbf{C}}^2]$ the first and second distortional (volume preserving) invariants, $\bar{\mathbf{C}} = \mathbf{C} J^{-2/3}$ the distortional part of the Cauchy Strain tensor $\mathbf{C} = \mathbf{F}^{\mathrm{T}}\mathbf{F}$, $J = (\det\ \mathbf{C})^{1/2}$ the determinant of the deformation gradient, $\mathbf{F} = \partial\boldsymbol{\varphi}/\partial\mathbf{x}_0$ the deformation gradient, $\boldsymbol{\varphi}$ the deformation, g the damage function, f the cyclic loading function, θ the volume change ratio, λ the Lagrange multiplier, c the void content and s_i are internal variables, and $\mathbf{x}_0$ the reference coordinates of a material point.

The distortional part of the strain energy function is represented by a Rivlin polynomial plus an exponential term on the first invariant $\bar{I}_1$ as suggested by Yeoh [3]

$$\bar{\phi} = \beta_1(\bar{I}_1 - 3) + \beta_2(\bar{I}_1 - 3)^2 + \beta_3(\bar{I}_1 - 3)^3 + \frac{\beta_4}{\beta_5}\left(1 + \mathrm{e}^{-\beta_5(\bar{I}_1 - 3)}\right), \tag{2}$$

where β_i are material coefficients.

The volume change ratio θ is represented by a multiplicative decomposition

$$\theta = \theta_{\mathrm{th}}\theta_{\mathrm{e}}\theta_{\mathrm{c}}, \tag{3}$$

where θ_{th} is the volume change ratio due to thermal effects, θ_{e} the volume change ratio due to elastic deformations and θ_{c} is the volume change ratio due to inelastic deformation. They are prescribed by the following formulas:

$$\theta_{\mathrm{th}} = (1 + \alpha(T - T_{\mathrm{rf}}))^3, \tag{4}$$

$$\theta_{\mathrm{c}} = 1 + c, \tag{5}$$

$$\theta_{\mathrm{e}} = \frac{\theta}{\theta_{\mathrm{th}}\theta_{\mathrm{c}}}, \tag{6}$$

where α is the coefficient of thermal expansion, T the body temperature, T_{rf} the reference temperature and c is the void content.

The dilatational part of the elastic strain energy density takes the following form:

$$\hat{\phi} = \frac{1}{2}K(\theta_e - 1)^2, \tag{7}$$

where K is the bulk modulus.

We now proceed to formulate the weak form of the equilibrium equations for elastic materials. Let Ω denote a continuum body in its reference configuration. Let $\partial\Omega$ be the boundary of Ω. Let $\partial\Omega_t$ be the part of the boundary where tractions are known and let $\partial\Omega_\varphi$ be the part of the boundary where deformations are prescribed. We assume that $\partial\Omega = \overline{\partial\Omega_t \bigcup \partial\Omega_\varphi}$, $\partial\Omega_t \bigcap \partial\Omega_\varphi = \emptyset$. The space of admissible configurations is defined as $\mathscr{V} = \{\boldsymbol{\varphi} \in \mathbf{W}^{1,s}(\Omega) : \Omega \to \mathbb{R}^3; \det \mathbf{F} > 0;\ \boldsymbol{\varphi} = \boldsymbol{\varphi}_0 \text{ on } \partial\Omega_\varphi\}$, where $\boldsymbol{\varphi}_0$ are the prescribed deformations on $\partial\Omega_\varphi$ and $\mathbf{W}^{1,s}(\Omega)$ is the Sobolev space ($s \geqslant 6$ to assure finite energy solutions) [4].

Suppose we have potential energy of external loading

$$\phi_{\text{ext}}(\boldsymbol{\varphi}) = \int_\Omega \rho_0 \mathbf{b} \cdot \boldsymbol{\varphi} + \int_{\partial\Omega_t} \mathbf{t} \cdot \boldsymbol{\varphi}, \tag{8}$$

where ρ_0 is the reference density, $\mathbf{b}$ the body force density, $\mathbf{t} = \mathbf{FSn}$ the traction per unit reference area prescribed on $\partial\Omega_t$, $\mathbf{S}$ the second Piola–Kirchhoff stress and $\mathbf{n}$ is the unit vector normal to the surface $\partial\Omega$ in the reference configuration.

Given a set of parameters $\{s_i, c, T\}$, the objective is to find a stationary point $\{\boldsymbol{\varphi}, \theta, \lambda\}$ of the following Lagrangian functional:

$$\Pi(\boldsymbol{\varphi}, \theta, \lambda) = \int_\Omega \phi(\boldsymbol{\varphi}, \theta, \lambda, s_i, c, T) - \phi_{\text{ext}}(\boldsymbol{\varphi}). \tag{9}$$

The space of admissible variations for φ is defined by

$$\mathscr{V}_0 = \{\boldsymbol{\varphi} \in \mathbf{W}^{1,s}(\Omega) : \Omega \to \mathbb{R}^3;\ \boldsymbol{\varphi} = \mathbf{0} \quad \text{on } \partial\Omega_\varphi\}. \tag{10}$$

Let $\mathscr{Q} = L^2(\Omega)$. The conditions for a stationary point $(\boldsymbol{\varphi}, \theta, \lambda)$ in (9) are given by the Euler–Lagrange equations.

Find $(\boldsymbol{\varphi}, \theta, \lambda) \in \mathscr{V} \times \mathscr{Q} \times \mathscr{Q}$ such that

$$\int_{\mathscr{B}} (\bar{\mathbf{S}}_e + \lambda J \mathbf{C}^{-1}) \cdot \delta\mathbf{E} - \delta\phi_{\text{ext}} = 0, \tag{11}$$

$$\int_{\mathscr{B}} (\hat{\sigma}_e - \lambda)\delta\theta = 0, \tag{12}$$

$$\int_{\mathscr{B}} (J - \theta)\delta\lambda = 0 \tag{13}$$

for all $(\delta\boldsymbol{\varphi}, \delta\theta, \delta\lambda) \in \mathscr{V}_0 \times \mathscr{Q} \times \mathscr{Q}$, where

$$\bar{\mathbf{S}}_e = gf\, \partial\bar{\phi}/\partial\mathbf{E} \tag{14}$$

is the stress due to distortional deformation, $\hat{\sigma}_e = \partial\hat{\phi}/\partial\theta$ is the stress due to dilatation and $\mathbf{E} = 1/2(\mathbf{C} - \mathbf{I})$ is the Green strain tensor. We refer to the pair $(\bar{\mathbf{S}}_e, \hat{\sigma}_e)$ as the elastic stresses.

2.2. Viscoelastic response

The viscoelastic response is obtained by using hereditary integrals on the elastic stresses, $\bar{\mathbf{S}}_e$ and $\hat{\sigma}_e$

$$\bar{\mathbf{S}}(t) = \int_0^t G_1(t-\tau)\frac{\partial\bar{\mathbf{S}}_e}{\partial\tau}\,\mathrm{d}\tau, \quad \hat{\sigma}(t) = \int_0^t G_2(t-\tau)\frac{\partial\hat{\sigma}_e}{\partial\tau}\,\mathrm{d}\tau, \tag{15}$$

where the pair $(\bar{\mathbf{S}}, \hat{\sigma})$ are the viscoelastic stresses and $G_1(t), G_2(t)$ are the relaxation moduli. For simplicity, we take $G(t) = G_1(t) = G_2(t)$.

The weak form of the equilibrium equations for our viscoelastic material is obtained by replacing the elastic stresses in (11) by the viscoelastic stresses.

At each time $t \in \mathbb{R}$, find $(\boldsymbol{\varphi}, \theta, \lambda) \in \mathscr{V} \times \mathscr{Q} \times \mathscr{Q}$ such that

$$\int_{\mathscr{B}} (\bar{\mathbf{S}} + \lambda J \mathbf{C}^{-1}) \cdot \delta \mathbf{E} - \delta \phi_{\text{ext}} = 0, \tag{16}$$

$$\int_{\mathscr{B}} (\hat{\sigma} - \lambda) \delta\theta = 0, \tag{17}$$

$$\int_{\mathscr{B}} (J - \theta) \delta\lambda = 0 \tag{18}$$

for all $(\delta\boldsymbol{\varphi}, \delta\theta, \delta\lambda) \in \mathscr{V}_0 \times \mathscr{Q} \times \mathscr{Q}$. Note that

$$\mathbf{S} = \bar{\mathbf{S}} + \lambda J \mathbf{C}^{-1} \tag{19}$$

is the second Piola–Kirchhoff stress. Explicit expressions for these equations are given in Appendix A.1. Note that this formulation allows taking into account the relaxation of the dilatational stress.

We next present the evolution equations for the internal variables.

2.3. The shift function

To take into account material property changes due to thermal effects, the actual time t in the relaxation functions is shifted to the reduced time ξ using a change of variable

$$\xi_t \equiv \xi(t) = \int_0^t \frac{\mathrm{d}\eta}{a_T}, \tag{20}$$

where $a_T = a(T(\eta))$ is the shift function and T is the body temperature.

2.4. Damage

When a propellant specimen is subjected to a tensile test, it is observed that there is a substantial increase in inelastic volume content, that is volume change that can be explained neither as elastic deformation nor as thermal deformation. This increase in inelastic volumetric deformation is associated with the formation and growth of voids due to dewetting of the solid particles in the elastomeric binder of the propellant. This effect is observed when the propellant is subjected to purely distortional deformations, as in granular materials. The rate of void growth substantially decreases with superimposed compressive pressure.

These observations can be described by the following evolution equation for the void content:

$$\dot{c} = \dot{\gamma} \mathrm{e}^{\hat{\sigma}_e/\omega_2}, \quad \gamma = \omega_1 \bar{I}_\gamma^n, \quad c(0) = 0, \tag{21}$$

where ω_1, ω_2 and n are material parameters and

$$\bar{I}_\gamma = \frac{1}{6}\sqrt{2\bar{I}_1^2 - 6\bar{I}_2}$$

is a measure of distortional deformation.

As the voids are formed, the material response to volumetric deformation softens. This effect is captured by softening the initial bulk modulus using the following evolution equation:

$$\frac{\mathrm{d}K(c)}{\mathrm{d}c} = -\frac{K}{1-c}(1 + \omega_3 K), \quad K(0) = K_0, \tag{22}$$

where K_0 is the initial bulk modulus, and ω_3 is a material parameter. The closed form solution for this evolution equation is given by

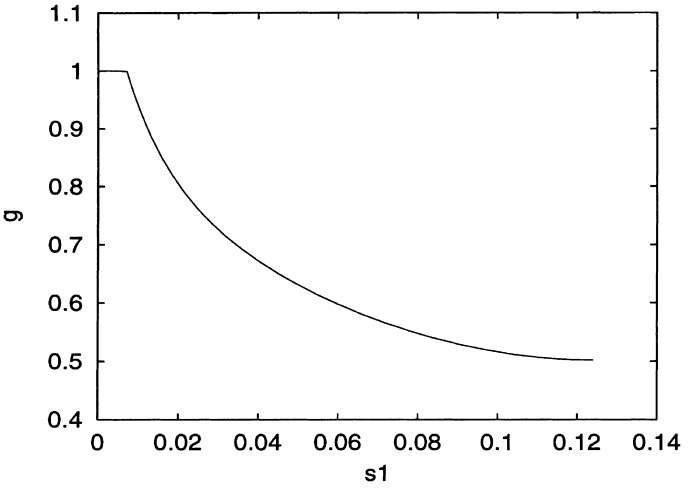

Fig. 1. Damage function.

$$K = \frac{K_0}{1 + \omega_3 K_0 c}(1 - c). \tag{23}$$

An important softening effect also occurs in the stresses. This effect is taken into account by reducing the elastic stress magnitude due to distortional deformation (14) with the *damage function, g* (see Fig. 1).

The damage function monotonically decreases with increasing void content. Its value is always positive but smaller than one. Even though the void content can decrease (21), the damage on the propellant is assumed to be irreversible, that is, the amount of damage s_1 is a nondecreasing function of the void content

$$s_1 = c_{\max} = \max_{0 \leqslant \tau \leqslant t} c(\tau), \quad g = g(s_1), \tag{24}$$

where $c_{\max}$ is the maximum void content over time, s_1 is the internal variable that measures the amount of damage, and g is the damage function.

2.5. Cyclic loading

During cyclic loading in a uniaxial tension test, the tensile stress in the stress–strain graph describes a closed path (Fig. 5). This effect is usually associated with work dissipation or hysteresis. Our material model correctly captures the overall effect of work dissipation. However, a more accurate prediction can be obtained by modifying the damage function with a new function which we call the *cyclic loading function*, f (Fig. 2).

The cyclic loading function f has three distinct branches, loading, unloading, f_u and reloading, f_r. Its values are always positive and smaller than one.

The values of the cyclic loading function largely depend on the amount of distortional deformation $\bar{I}_\gamma$

$$s_2 = \frac{\bar{I}_\gamma}{\bar{I}_\gamma^{\mathrm{l}}}, \tag{25}$$

where s_2 is an internal variable and $\bar{I}_\gamma^{\mathrm{l}}$ is the maximum $\bar{I}_\gamma$ during loading. We define $\bar{I}_\gamma^{\mathrm{u}}$ as the minimum $\bar{I}_\gamma$ during unloading

$$f = \begin{cases} 1 & \text{loading}, \\ f_u & \text{unloading}, \\ f_u + s_3(f_r - f_u) & \begin{cases} \text{reloading}, \\ \text{unloading from reloading}, \end{cases} \end{cases} \tag{26}$$

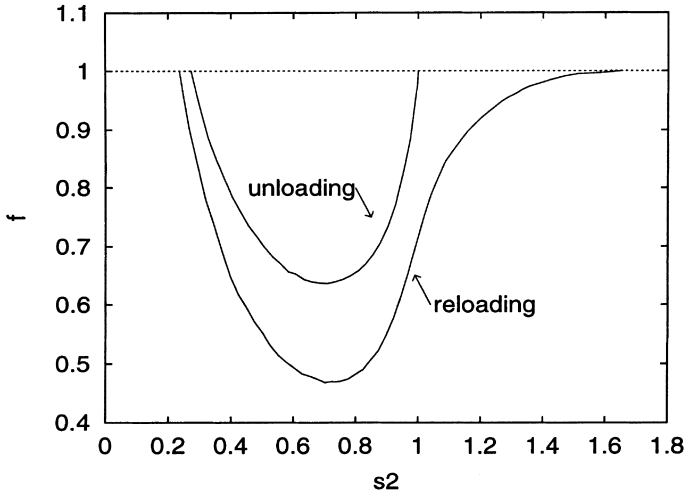

Fig. 2. Cyclic loading function.

where s_3 is defined as

$$s_3 = \begin{cases} (\bar{I}_\gamma - \bar{I}_\gamma^{\mathrm{u}})/(\bar{I}_\gamma^{\mathrm{l}} - \bar{I}_\gamma^{\mathrm{u}}), & \bar{I}_\gamma^{\mathrm{u}} < \bar{I}_\gamma < \bar{I}_\gamma^{\mathrm{l}}, \\ 1, & \bar{I}_\gamma > \bar{I}_\gamma^{\mathrm{l}}. \end{cases} \tag{27}$$

These definitions are intended to smooth out the transition between the different branches.
The reloading path blends with the loading path when $s_2 \geqslant 1.4$. In that case, $\bar{I}_\gamma^{\mathrm{l}}$ is reset to $\bar{I}_\gamma$ (Fig. 2).

3. Computational methods

3.1. Intermediate configurations

The relaxation function is expressed in terms of a Prony series expansion

$$G(t) = G_\infty + \sum_{i=1}^{m} G_i \mathrm{e}^{-t/\tau_i}, \tag{28}$$

where G_∞ is the equilibrium (long term) modulus, and τ_i are the relaxation times.
Using (28) in (15), we obtain the following expansion:

$$(\bar{\mathbf{S}}, \hat{\sigma}) = G_\infty (\bar{\mathbf{S}}, \hat{\sigma})_{\mathrm{e}} + \sum_{i=1}^{m} G_i \int_0^t \mathrm{e}^{(\xi_\tau - \xi_t)/\tau_i} \frac{\partial (\bar{\mathbf{S}}, \hat{\sigma})_{\mathrm{e}}}{\partial \tau} \, \mathrm{d}\tau. \tag{29}$$

The reduced time is decomposed as

$$\xi_\tau - \xi_t = \xi_\tau - \xi_n + \xi_n - \xi_t, \quad \Delta\xi(t) = \xi_n - \xi_t, \tag{30}$$

where subindex n is the time corresponding to a known intermediate configuration. For simplicity, it is convenient to introduce an auxiliary viscoelastic stress variable

$$\mathbf{H}_t^i = \int_0^t \mathrm{e}^{(\xi_\tau - \xi_t)/\tau_i} \frac{\partial (\bar{\mathbf{S}}, \hat{\sigma})_{\mathrm{e}}}{\partial \tau} \, \mathrm{d}\tau. \tag{31}$$

Using (31) in (29), we obtain

$$(\bar{\mathbf{S}},\hat{\sigma})(t) = G_\infty(\bar{\mathbf{S}},\hat{\sigma})_{\mathrm{e}}(t) + \sum_{i=1}^{m} G_i \mathbf{H}_t^i. \tag{32}$$

Using (30) into (31) and (32), we get

$$(\bar{\mathbf{S}},\hat{\sigma})(t) = G_\infty(\bar{\mathbf{S}},\hat{\sigma})_{\mathrm{e}}(t) + \sum_{i=1}^{m} G_i \mathrm{e}^{(\Delta\xi)/\tau_i}\left[\int_0^t \mathrm{e}^{(\xi_\tau-\xi_n)/\tau_i}\frac{\partial(\bar{\mathbf{S}},\hat{\sigma})_{\mathrm{e}}}{\partial\tau}\,\mathrm{d}\tau\right]. \tag{33}$$

Finally, expressing the viscoelastic stresses with respect to an intermediate configuration, we obtain

$$(\bar{\mathbf{S}},\hat{\sigma})(t) = G_\infty(\bar{\mathbf{S}},\hat{\sigma})_{\mathrm{e}}(t) + \sum_{i=1}^{m} G_i\left[\mathrm{e}^{(\Delta\xi)/\tau_i}\mathbf{H}_n^i + \int_n^t \mathrm{e}^{(\xi_\tau-\xi_t)/\tau_i}\frac{\partial(\bar{\mathbf{S}},\hat{\sigma})_{\mathrm{e}}}{\partial\tau}\,\mathrm{d}\tau\right]. \tag{34}$$

Note that from (34), to evaluate the viscoelastic stresses at time t, it is sufficient to know the elastic stresses at time t, the history-dependent viscoelastic stress tensor $\mathbf{H}_n^i$ carried from some previous configuration at time n, and the value of the integral from previous time n to present time t.

3.2. Time stepping algorithms

In this section, we are concerned with the time integration algorithms for the viscoelastic stresses in (34). We could assume that $(\bar{\mathbf{S}},\hat{\sigma})_{\mathrm{e}}$ vary linearly within a time increment so that (35) holds

$$\frac{\partial(\bar{\mathbf{S}},\hat{\sigma})_{\mathrm{e}}}{\partial\tau} = \frac{1}{\Delta t}((\bar{\mathbf{S}},\hat{\sigma})_{\mathrm{e}}(t) - (\bar{\mathbf{S}},\hat{\sigma})_{\mathrm{e}}(n)). \tag{35}$$

Using (35) in (34) we get

$$(\bar{\mathbf{S}},\hat{\sigma})(t) = G_\infty(\bar{\mathbf{S}},\hat{\sigma})_{\mathrm{e}}(t) + \sum_{i=1}^{m} G_i\left[\mathrm{e}^{(\Delta\xi)/\tau_i}\mathbf{H}_n^i + \frac{1}{\Delta t}((\bar{\mathbf{S}},\hat{\sigma})_{\mathrm{e}}(t) - (\bar{\mathbf{S}},\hat{\sigma})_{\mathrm{e}}(n))\int_n^t \mathrm{e}^{(\xi_\tau-\xi_t)/\tau_i}\,\mathrm{d}\tau\right]. \tag{36}$$

The exponential term is integrated analytically. The terms in brackets

$$\mathbf{H}_t^i = \mathrm{e}^{\Delta\xi/\tau_i}\mathbf{H}_n^i + \frac{1}{\Delta t}((\bar{\mathbf{S}},\hat{\sigma})_{\mathrm{e}}(t) - (\bar{\mathbf{S}},\hat{\sigma})_{\mathrm{e}}(n))\int_n^t \mathrm{e}^{(\xi_\tau-\xi_t)/\tau_i}\,\mathrm{d}\tau \tag{37}$$

are stored as history variables.

The void content is integrated with a forward Euler scheme. The value of $\dot{\bar{I}}_\gamma^n$ is extrapolated. Thus we have

$$c(t) = c(n) + \Delta\gamma(n)\mathrm{e}^{\hat{\sigma}_{\mathrm{e}}(n)/\omega_2}, \tag{38}$$

where

$$\Delta\gamma(n) = \omega_1(\bar{I}_\gamma^n(n) - \bar{I}_\gamma^n(n-1)). \tag{39}$$

This integration choice greatly simplifies the complexity of our integration scheme. After applying the finite element method, the resulting tangent stiffness is symmetric and it does not depend on changes in the damage function during the increment.

After obtaining $c(t)$, the internal value s_1 (24), the damage function (24), and the bulk modulus K (23) are evaluated. The cyclic loading function is evaluated using (26) based on the values of the internal variables s_2 (25) and s_3 (27).

Using the values of K, f, and g, the elastic stresses are obtained using (A.3) and (A.7).

3.3. Finite element approximations

The standard isoparametric finite element approximations for (16)–(18) are constructed using, for each finite element Ω_e, shape functions N [5]. The deformations φ are discretized with

$$\mathscr{V}^h = \left\{ \boldsymbol{\varphi}^h \in \mathscr{V} : \boldsymbol{\varphi}^h|_{\Omega_e} \equiv \boldsymbol{\varphi}^e = \sum_{\alpha=1}^{n_\varphi} N_\varphi^\alpha \boldsymbol{\varphi}_\alpha^e \right\}, \tag{40}$$

where $\boldsymbol{\varphi}_\alpha^e$ are the nodal point coordinates at time t corresponding to the deformed configuration and n_φ is the number of shape functions for each element. Note that the $\boldsymbol{\varphi}_\alpha^e$ corresponding to displacement boundary conditions are known.

The volume change ratio and Lagrange multipliers are discretized with

$$\mathscr{Q}^h = \left\{ p^h \in \mathscr{Q} : p^h|_{\Omega_e} \equiv p^e = \sum_{\alpha=1}^{n_p} N_p^\alpha p_\alpha^e \right\}, \tag{41}$$

where p_α^e are the unknown volume change ratio or Lagrange multiplier coefficients and n_p is the number of volume change ratio or Lagrange multiplier unknowns per element.

In the numerical work, we used second-order elements. For $\{N_\varphi\}$, we chose continuous triquadratic polynomials (biquadratic in 2D), and for $\{N_\lambda\}$, and $\{N_\theta\}$ we chose linear polynomials that are discontinuous at inter-element boundaries.

After replacing the approximations (40) and (41) in the equilibrium equations (16)–(18) using standard finite element techniques, the problem is reduced to solving a set of algebraic nonlinear equations $\mathbf{R}$

$$\mathbf{R}(\varphi_i, \lambda_j, \theta_k) = \mathbf{0}, \quad i = 1, 3 * n_{no}, \;\; j = 1, 3 * n_{el}, \;\; k = 1, 3 * n_{el}, \tag{42}$$

where n_{no} is the number of nodal points and n_{el} is the number of elements. To solve the equations we use the Newton–Raphson (N–R) method. Recall that N–R applied to a given set of equations $\mathbf{R}(\mathbf{z}) = \mathbf{0}$ consists of finding the root $\mathbf{z}$ with the following iterate updates:

$$\mathbf{z}_{l+1} = \mathbf{z}_l - \left(\frac{\partial \mathbf{R}}{\partial \mathbf{z}} \right)_l^{-1} \mathbf{R}_l, \tag{43}$$

the right-hand side being evaluated at $\mathbf{z}_l$. Expressions for the Jacobian are given in Appendix A.2.

4. Material model calibration

In this section, we discuss the procedure to calibrate the propellant. Material tests provided the following information:

- Initial bulk modulus.
- Coefficient of thermal expansion.
- Stress vs. time data from short-term relaxation tests at 0 psig and 5% strain. The tests are for several temperatures ranging from −75°F to 170°F, with a duration of 17 min.
- Stress vs. time data from long-term relaxation test at 0 psig, 5% strain and 75°F with a duration of 30 days.
- Stress, dilatation and strain data from uniaxial tension tests with monotonic loading and cyclic loading at several external pressures from 0 to 1000 psig, at three different strain rates 0.071, .71 and 7.1 [1/min].

4.1. The Shift function and the Prony series

The relaxation modulus was obtained from a series of relaxation curves at different temperatures by assuming thermorheologically simple behaviour. The time–temperature equivalence implied by this assumption consists of rescaling the time for each curve using a shift function. The reference temperature was

chosen as 75°F. The constant temperature relaxation curves were horizontally shifted on a log–log scale so as to form a single curve called the master modulus. The shift function, determined by the horizontal shift, was mathematically represented by a multilinear function.

The master curve was represented by a Prony series approximation. The procedure consisted of selecting the characteristic times τ_i one decade apart, and then finding the coefficients G_i, using a least-squares technique.

4.2. The hyperelastic coefficients

The hyperelastic coefficients were obtained from the uniaxial tension test at 1000 psig. Since the inelastic dilatation at that pressure level is insignificant, it was assumed that no damage occurs, so the propellant is considered a viscoelastic material without damage, i.e., $g = 1$. The hyperelastic coefficients were adjusted with an optimization program that computes the best fit for the tensile test, verifying that the Rivlin polynomial coefficients produce a material model that is stable (all its eigenvalues positive) within the 40% deformation range. The uniaxial stress–strain data and the Prony coefficients are input to the optimization process.

4.3. The damage and cyclic loading function calibration

The damage and cyclic loading functions were calibrated with the help of a specifically designed numerical algorithm inside the finite element program. We started with the damage function. The procedure consisted of assuming an initial guess for the dilatation parameters (Table 1). With the initial guess, a new damage function was calculated so that the viscoelastic stress matched the experimental stress $S^{\exp}_{11\ \mathrm{mon}}$ from the monotonic uniaxial test at 0 psig and 0.71 [1/min] strain rate. The algorithm is outlined as follows:

Set

$$g(s_1(0)) = 1, \qquad f = 1. \tag{44}$$

The elastic stress at time t is given by

$$\bar{S}_{\mathrm{e}\,11}(t) = g(s_1(t))\frac{\partial \bar{\phi}}{\partial E_{11}}(t). \tag{45}$$

Using (45) in (19) and (36), we get

$$S^{\exp}_{11\ \mathrm{mon}}(t) = g(s_1)\frac{\partial \bar{\phi}}{\partial E_{11}}(t)\left[G_\infty + \sum_{i=1}^{m}\frac{G_i}{\Delta t}\int_n^t \mathrm{e}^{(\xi_\tau-\xi_t)/\tau_i}\,\mathrm{d}\tau\right] + \sum_{i=1}^{m}\frac{G_i}{\Delta t}\left[\mathrm{e}^{(\Delta\xi)/\tau_i}H^i_{n\,11} - \bar{S}_{\mathrm{e}\,11}(n)\int_n^t \mathrm{e}^{(\xi_\tau-\xi_t)/\tau_i}\,\mathrm{d}\tau\right] + \lambda(t)J(t)C^{-1}_{11}(t). \tag{46}$$

We solve for $g(t)$. $H^i_{11}(t)$ is updated using (37) for the next step. After the time integration is completed, the coefficients of the dilatation model are adjusted and the procedure is repeated. Typically, it takes just a few cycles of the outlined procedure to obtain a good fit for the damage function and dilatation parameters.

For the adjustment of the cyclic loading function, we use an expression similar to (46) but this time we allow $f = f(s_2(t), s_3(t))$ to vary. We use the the calibrated damage function and dilatational parameters obtained from previous step. To adjust the cyclic loading function, we use the experimental stress $S^{\exp}_{11\ \mathrm{cyc}}$ from the cyclic uniaxial test at 0 psig and 0.71 [1/min] strain rate.

Set

$$f(s_2(0), s_3(0)) = 1. \tag{47}$$

The elastic stress at time t is given by

$$\bar{S}_{\mathrm{e}\,11}(t) = g(s_1(t))f(s_2(t), s_3(t))\frac{\partial \bar{\phi}}{\partial E_{11}}(t). \tag{48}$$

The uniaxial stress for cyclic loading is given by

$$S_{11\,\mathrm{cyc}}^{\mathrm{exp}}(t) = g(s_1)f(s_2,s_3)\frac{\partial\bar{\phi}}{\partial E_{11}}(t)\left[G_\infty + \sum_{i=1}^{m}\frac{G_i}{\Delta t}\int_n^t \mathrm{e}^{(\xi_\tau-\xi_t)/\tau_i}\,\mathrm{d}\tau\right] + \sum_{i=1}^{m}\frac{G_i}{\Delta t}\left[\mathrm{e}^{(\Delta\xi)/\tau_i}H_{n\,11}^{i} - \bar{S}_{\mathrm{e}\,11}(n)\int_n^t \mathrm{e}^{(\xi_\tau-\xi_t)/\tau_i}\mathrm{d}\tau\right] + \lambda(t)J(t)C_{11}^{-1}(t). \tag{49}$$

This time we solve for f.

5. Examples

In this section, we first present some results to illustrate the performance of the model in representing the mechanical behaviour of a solid propellant under simple loading conditions. Next, we present the solution

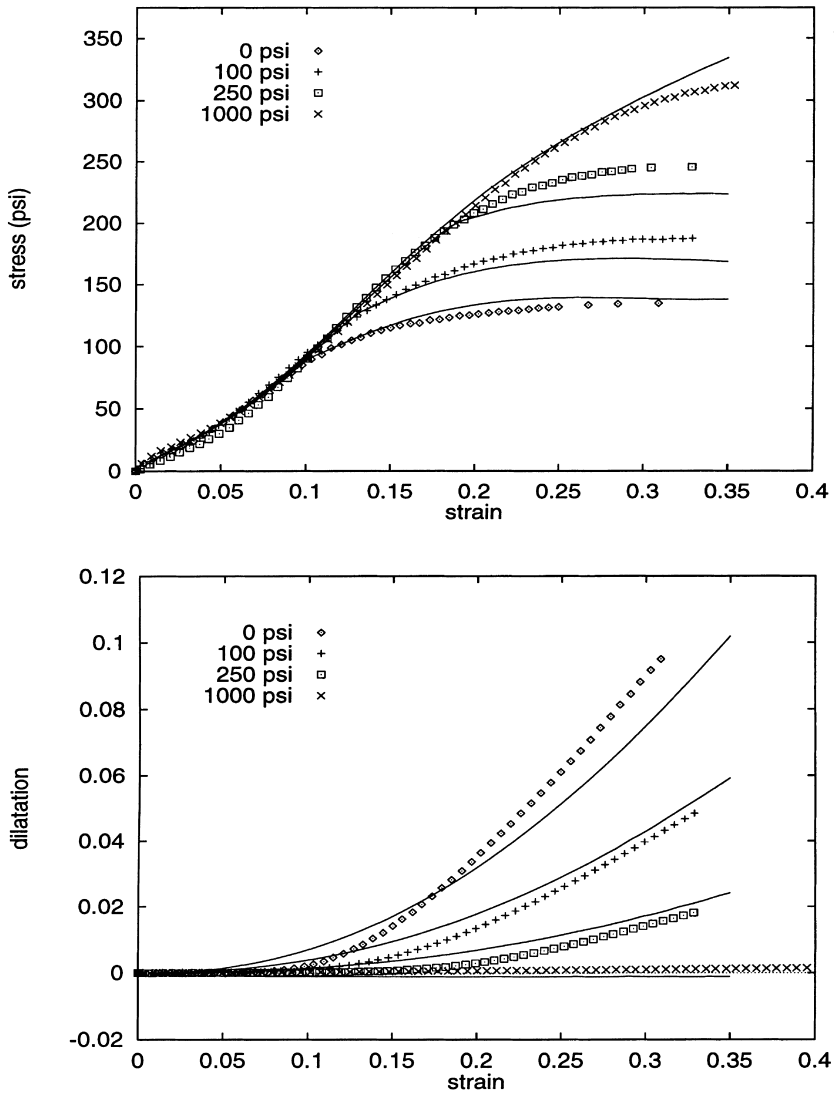

Fig. 3. Pressure effect on stress and dilatation for uniaxial tensile tests at 0.714 min^{-1}.

of two problems for a solid rocket motor to demonstrate the overall performance of the nonlinear viscoelastic analysis that we developed. The analyses were carried out through the finite element code TEXPAC [6].

5.1. Uniaxial test

We calibrated the model for the Space Shuttle redesigned solid rocket motor (RSRM) propellant, TP-H1148. The experimental data used in both calibration and verification of the model have been provided by Nelson [7]. The procedure for the calibration which is outlined in the previous sections resulted in material parameter values given in Table 1 and Figs. 1 and 2.

Fig. 3 shows test data (symbols) and model prediction (lines) of stress and dilatation vs. axial strain for uniaxial tests run with several values of superimposed hydrostatic pressure. We note that the calibration procedure used the 1000 psi stress data and the 0 psi dilatation data only. The agreement between measured and predicted response is well within the range of specimen to specimen variation of test results.

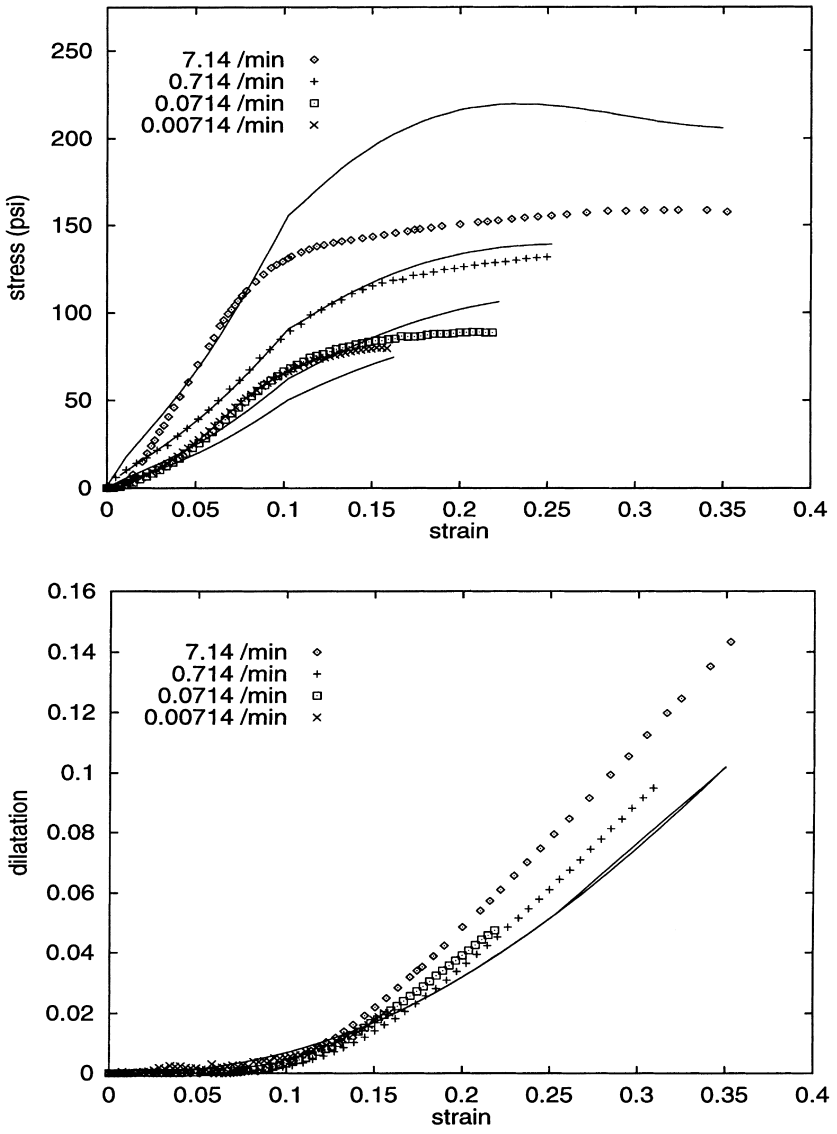

Fig. 4. Strain rate effect on stress and dilatation for uniaxial constant strain rate tests at ambient pressure.

Table 1
Relaxation modulus and other material constants for TP-H 1148 solid rocket propellant

G_i (psi)	τ_i (min)	Coefficients of $\overline{\phi}$	Dilatation parameters
5976.86	0.4754E − 5	$\beta_1 = 0.2863$ psi	$\omega_1 = 1.5$
3457.01	0.4754E − 4	$\beta_2 = 0.0$	$\omega_2 = 0.222$
1903.49	0.4754E − 3	$\beta_3 = 0.0$	$\omega_3 = 0.501$
971.28	0.4754E − 2	$\beta_4 = 0.1863$ psi	$n = 2$
487.53	0.4754E − 1	$\beta_5 = 17.60$	$K_0 = 1108.73$ psi
142.83	0.4754E + 0		
87.57	0.4754E + 1		
86.55	0.4754E + 2		
104.49	0.4754E + 3		
177.83	0.4754E + 4		
$G_{eq} = 133.83$			

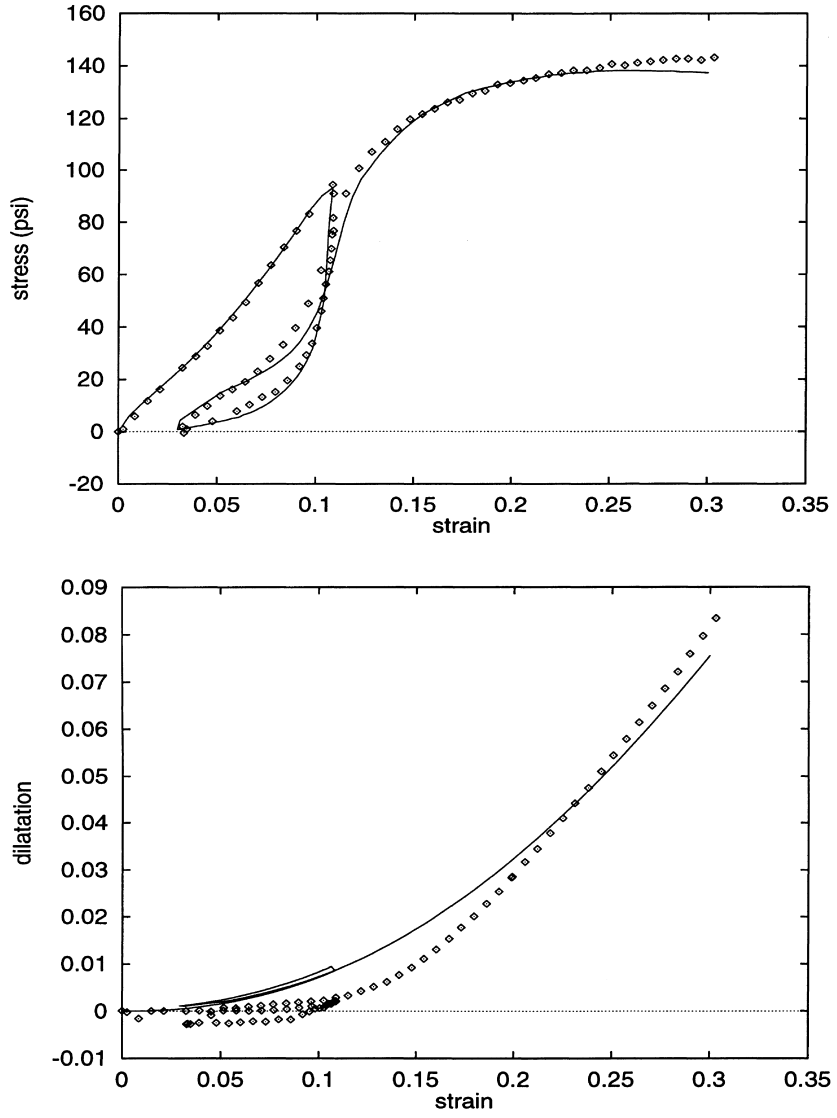

Fig. 5. Uniaxial cyclic tensile test at 0.714 min^{-1}, with unloading at 10% strain.

Fig. 4 shows test data and model prediction stresses and dilatations for uniaxial tests run at several strain rates. The dilatation (and, therefore, the damage) appears to be almost completely insensitive to strain rate and no strain rate effect is included in the damage model. The agreement between data and prediction is fair for dilatation but marginal for stress values. Dilatation measurements at very low and very high strain rates can be difficult. We conclude that the dependence (or lack thereof) of damage on strain rate remains an open issue.

Fig. 5 shows test data and model prediction of stress and dilatation for a uniaxial test that comprises cycle of unloading and reloading. The agreement is adequate.

5.2. Flexible case motor

We now present the finite element analysis of a subscale flexible case rocket motor (FCM) under various loading conditions, and compare the predictions with the test data. The subscale motors that we consider were cast with TP-H1148 propellant discussed above. The examples that we present consisted of pressurizing the FCM with two different methods and are significant in demonstrating the validity of our constitutive model under multiaxial stress and strain states and the accuracy of the structural analysis methodology. The experimental data for the FCM have been provided by Collingwood et al. [8].

5.2.1. Motor description

The FCM case consists of a steel tube 12.5 in. long, with a 3.0 in. inside diameter. The wall thickness is 0.080 in. with a build-up to 0.125 in. at the ends. The motor was cast with a full-length center-perforated grain with a 0.5 in. diameter bore. The steel case and the propellant were the only components; no insulation or liner was used. Instrumentation for the FCM consists of normal stress gages between the case and propellant at the center of the case; three bore displacement gages, one at the center and one at each of the quarter points; a sensor measuring grain end displacement at the bore; three hoop strain gages on the

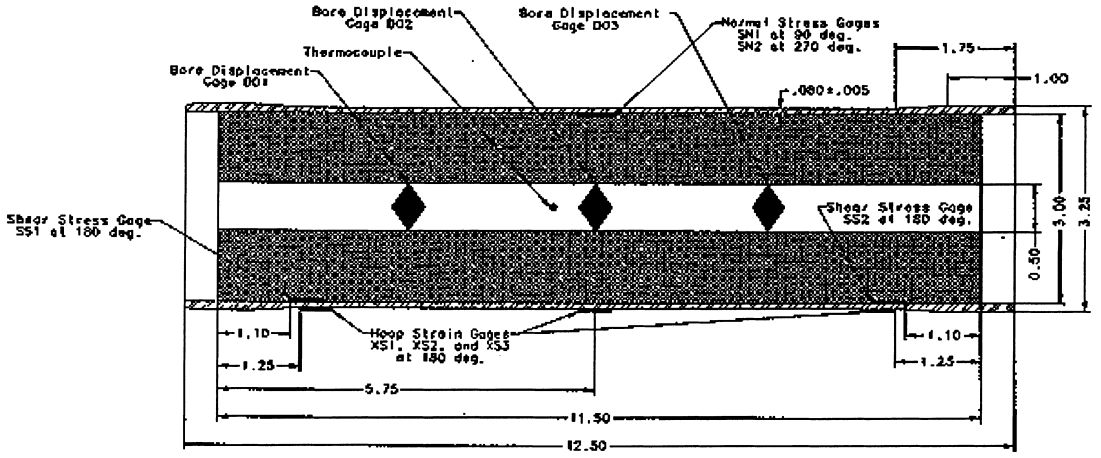

Fig. 6. Flexible case motor.

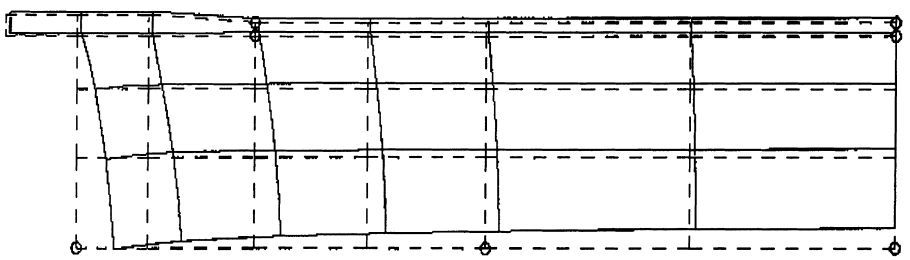

Fig. 7. Deformed and undeformed (dashed) shape of FCM.

outside of the case at the center and approximately mid-way between the grain end and a quarter point, and two shear stress gages between case and grain, mid-way between the grain end and a quarter point. Fig. 6 contains a sketch of the FCM motor showing its dimensions and approximate gage locations.

For the finite element analysis, one half of an axisymmetric slice of the FCM was modeled using 9-node quadrilateral elements. The case consisted of seven elements with one element through the thickness. The grain was modeled with 18 elements in a nonuniform grid of six elements axially and three elements through

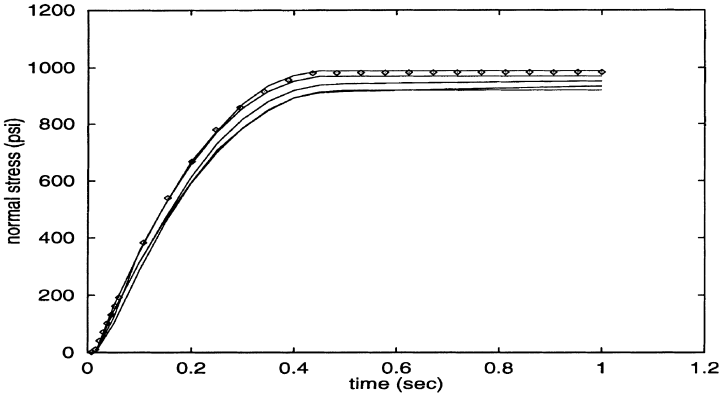

Fig. 8. FCM rapid pressurization: normal stress.

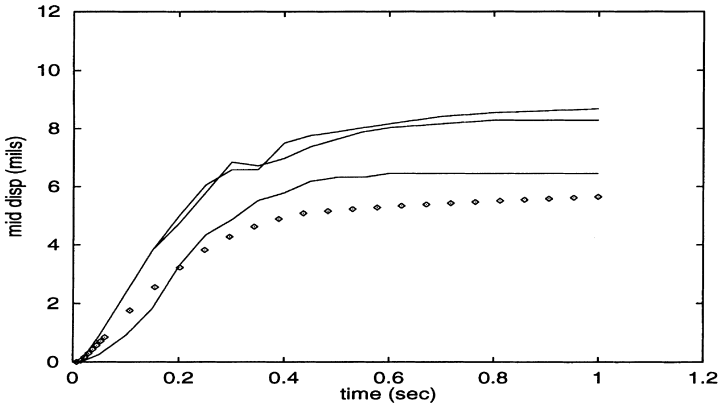

Fig. 9. FCM rapid pressurization: mid-point bore displacement.

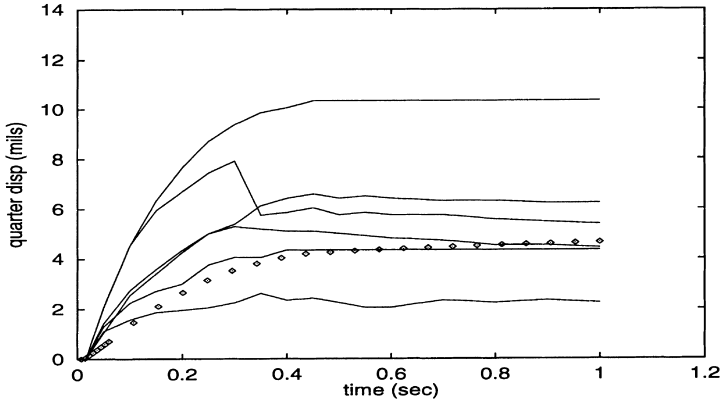

Fig. 10. FCM rapid pressurization: quarter-point bore displacement.

the thickness. The steel case was considered to be linear and isotropic for the analysis. Young's modulus for the steel was 29×10^6 psi, Poisson's ratio was 0.3.

We also studied a finite element mesh consisting of 375 elements for the grain and 27 elements for the case. The results that we will next present were not affected by this finer mesh. Typical deformed and undeformed configurations are shown in Fig. 7, where the locations corresponding to the gages are shown.

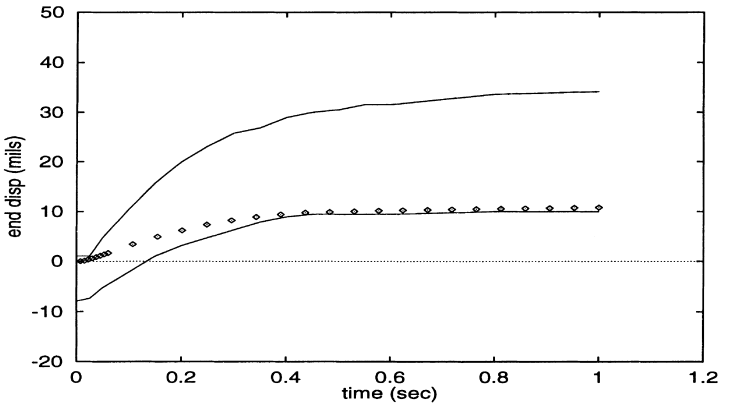

Fig. 11. FCM rapid pressurization: grain end displacement.

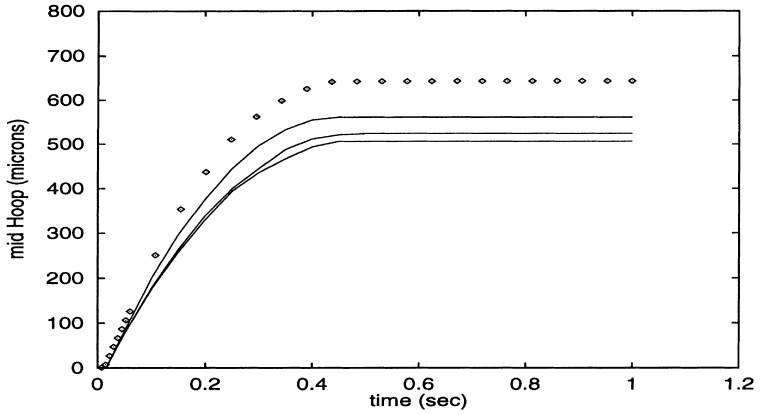

Fig. 12. FCM rapid pressurization: mid-point external case strain.

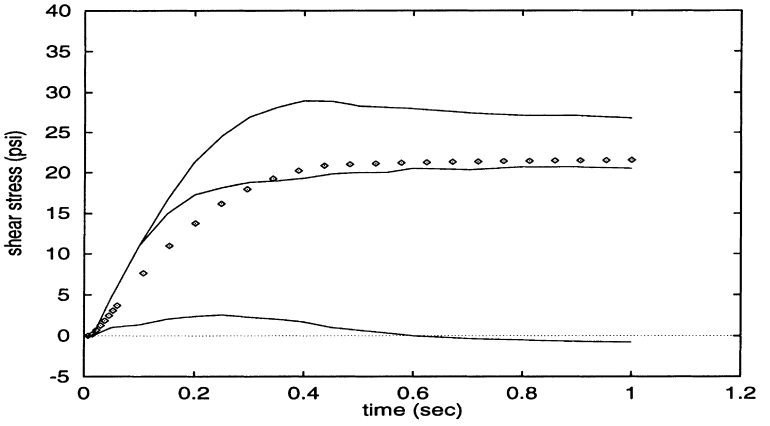

Fig. 13. FCM rapid pressurization: shear stress.

5.2.2. FCM-rapid pressurization test

In this series of three tests, loading on the motor consisted of internal pressure rising to a peak of approximately 1000 psi over about 1 s. The predicted results (symbols) and the measured data (lines) are shown in Figs. 8–13 from which we can draw the following conclusions:

- *Normal stress.* Fig. 8 shows the predicted and measured value of normal stress at the case-propellant bond line. There is very little dispersion in the measured traces. The value of this stress tracks the value of applied pressure. The predicted result is in excellent agreement with the measured values.
- *Bore displacement.* Bore displacement values for mid point and quarter point gage locations are shown in Figs. 9 and 10, respectively. There is a large amount of scatter in the test data although almost all gages show a similar response. The predicted values are in reasonable agreement.
- *Grain end displacement*. (Fig. 11) prediction at the bore overlays one of the test curves. However, since the data showed large scatter among the three motors (not all shown in the Figure), this may not be conclusive evidence.
- *Hoop strain.* (Fig. 12) results are slightly above the test data. The discrepancy could be due to the inaccuracy of the case thickness. The conclusions are the same both at the center and at the quarter points.
- *Shear stress* (Fig. 13) comparisons are adequate considering the data scatter which maybe due to sensitivity of results to gage positioning. One gage apparently malfunctioned.

5.2.3. FCM-rapid depressurization test

In this loading, the motor was pressurized both internally and externally to a pressure of approximately 1000 psi; the external pressure was then removed during a time span of about 1 s, while the internal pressure

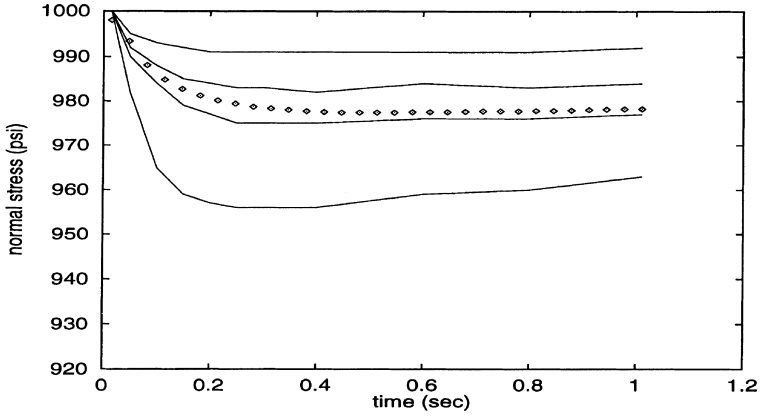

Fig. 14. FCM rapid depressurization: normal stress.

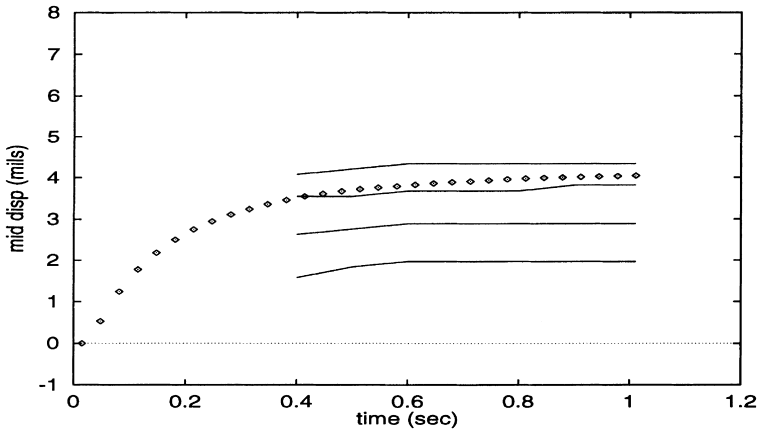

Fig. 15. FCM rapid depressurization: mid-point bore displacement.

was held constant. In the analysis the initial internal and external pressurization was applied as a linear ramp loading over a time period of 2 min.

Analysis results (symbols) and test data (lines) are shown in Figs. 14–18 and can be summarized as follows:

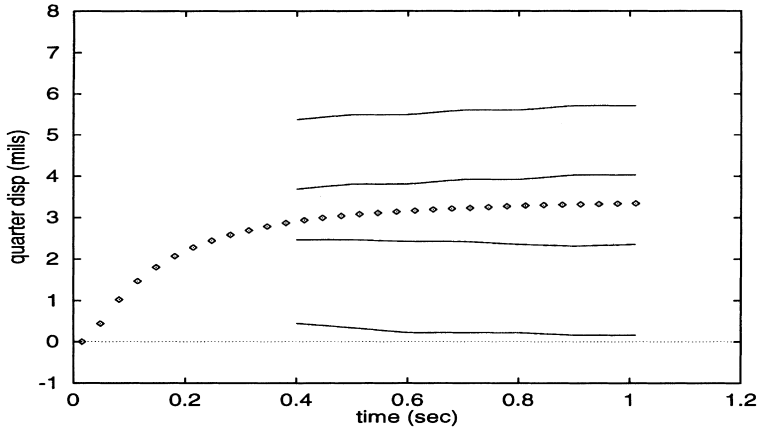

Fig. 16. FCM rapid depressurization: quarter-point bore displacement.

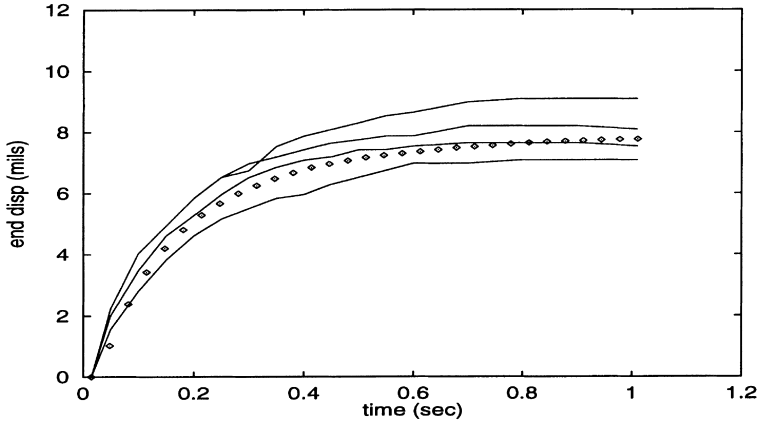

Fig. 17. FCM rapid depressurization: grain end displacement.

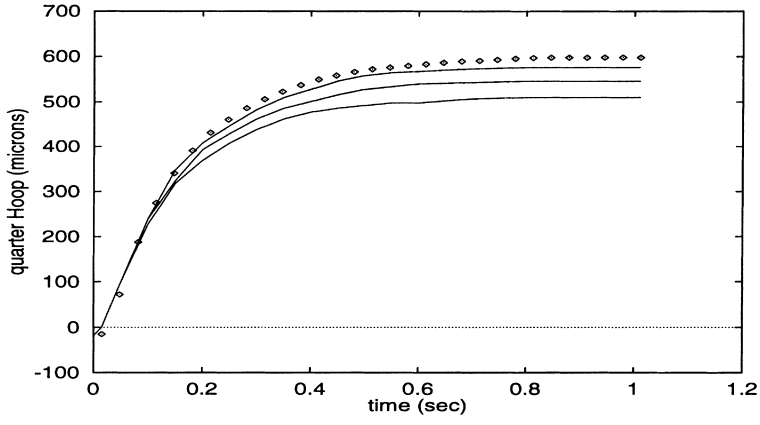

Fig. 18. FCM rapid depressurization: 'quarter-point' external case strain.

- For valid comparison of *normal stress* (Fig. 14), both the data and analysis results were shifted to 1000 psi at zero time which was defined as the initiation of depressurization. Predictions show good correlation with the gage data, which show a surprising amount of scatter.
- *Bore displacement* (Figs. 15 and 16) test data as well as the predictions were shifted to zero displacement at zero time. The initial part of test results is not shown because of difficulty in reading the data. The agreement between predicted and average test data is quite good both at the center and the quarter points.
- *Grain end displacement* (Fig. 17) results from both the test and the analysis were also shifted to zero displacement at zero time. As with the bore displacement, the agreement between predictions and data is quite good.
- As in the pressurization case, *Hoop strain* (Fig. 18) is slightly overpredicted. The conclusions are the same both at the center and at the 'quarter' points.

6. Concluding remarks

A formulation for the analysis of viscoelastic materials with damage has been developed. The formulation has been implemented in a finite element code, which supports large deformations, large rotations and thermal effects. The resulting algebraic equations from the FEM are solved with a time marching technique that utilizes Newton–Raphson equilibrium iterations. The tangent stiffness (Jacobian) derived from the numerical formulation is symmetric and has been calculated exactly, resulting in an efficient numerical implementation. The model can be calibrated using data from a reasonable number of tests. The calibration of the model using solid rocket propellant test data illustrates the procedure.

The performance of the model is illustrated for uniaxial loading at various pressure levels, strain rates and loading paths. The model represents the propellant behaviour reasonably well except for the stress at a high strain rate. This implies the dependence of the damage function on the strain rate. The dilatation response of the propellant calibrated in this paper does not show significant rate dependence. Reported in the literature, however, are other propellant data where a considerable rate dependence is observed. The model is currently being revised to address this issue.

The overall performance of the viscoelastic analysis is illustrated for the pressurization/depressurization of a subscale flexible rocket motor. The predictions for normal stress and displacements at various points of the motor correlate well with the experimental data. The results encourage the employment of the nonlinear viscoelastic stress analysis method that we described to predict the response of the full-scale motor under various operational loadings.

Acknowledgements

The authors gratefully acknowledge Thiokol for the use of the test data and Dr. Trent Miller of Mechanics Software for many useful discussions throughout the course of this work.

Appendix A

In this appendix, we have condensed the equations needed to implement the material model in a finite element method.

A.1. Strains and stresses

The elastic stress, $\bar{\mathbf{S}}_e$, due to distortional deformation is obtained by differentiating the distortional part of the elastic energy density with respect to the Green strain tensor

$$\bar{\mathbf{S}}_e = gf\frac{\partial\bar{\phi}}{\partial\mathbf{E}} = gf\frac{\partial\bar{\phi}}{\partial\bar{I}_1}\frac{\partial\bar{I}_1}{\partial\mathbf{E}} = 2gf\frac{\partial\bar{\phi}}{\partial\bar{I}_1}\frac{\partial\bar{I}_1}{\partial\mathbf{C}}, \tag{A.1}$$

since $\mathrm{d}\mathbf{E} = 1/2\,\mathrm{d}\mathbf{C}$. The term $\partial\bar{\phi}/\partial\bar{I}_1$ in (A.1) is

$$\frac{\partial\bar{\phi}}{\partial\bar{I}_1} = \beta_1 + 2\beta_2(\bar{I}_1 - 3) + 3\beta_3(\bar{I}_1 - 3)^2 - \beta_4 \mathrm{e}^{-\beta_5(\bar{I}_1 - 3)}. \tag{A.2}$$

So

$$\bar{\mathbf{S}}_{\mathrm{e}} = 2gf\left(\beta_1 + 2\beta_2(\bar{I}_1 - 3) + 3\beta_3(\bar{I}_1 - 3)^2 - \beta_4 \mathrm{e}^{-\beta_5(\bar{I}_1 - 3)}\right)\frac{\partial\bar{I}_1}{\partial\mathbf{C}}, \tag{A.3}$$

where

$$\frac{\partial\bar{I}_1}{\partial\mathbf{C}} = \frac{\mathscr{I}}{I_3^{1/3}} - \frac{1}{3}\frac{\mathscr{I}\cdot\mathbf{C}}{I_3^{1/3}}\mathbf{C}^{-1}. \tag{A.4}$$

This derivation has used the fact that

$$\mathrm{d}I_1 = \mathrm{tr}(\mathrm{d}\mathbf{C}) = \mathscr{I}\cdot\mathrm{d}\mathbf{C}, \quad \mathrm{d}I_3 = I_3(\mathbf{C}^{-1}\cdot\mathrm{d}\mathbf{C}) \tag{A.5}$$

and

$$\mathrm{d}\bar{I}_1 = \frac{\mathscr{I}\cdot\mathrm{d}\mathbf{C}}{I_3^{1/3}} - \frac{1}{3}\frac{\mathscr{I}\cdot\mathbf{C}}{I_3^{1/3}}(\mathbf{C}^{-1}\cdot\mathrm{d}\mathbf{C}), \tag{A.6}$$

where $\mathscr{I}$ is the second-order identity tensor.

The elastic stress due to dilatation is obtained by differentiating the stored energy function with respect to the volume change ratio (7)

$$\hat{\sigma}_{\mathrm{e}} = \frac{\partial\phi}{\partial\theta} = \frac{K}{\theta_{\mathrm{th}}\theta_{\mathrm{c}}}\left(\frac{\theta}{\theta_{\mathrm{th}}\theta_{\mathrm{c}}} - 1\right). \tag{A.7}$$

A.2. The Jacobian

The Jacobian, also referred as the tangent stiffness, is used in the Newton–Raphson algorithm (43). It is the increment of the equilibrium equations

$$\begin{aligned}\mathrm{d}\mathbf{R} = &\int_{\mathscr{B}}(\mathrm{d}\bar{\mathbf{S}}\cdot\delta\mathbf{E} + \mathrm{d}\hat{\sigma}\delta\theta) + \int_{\mathscr{B}}\bar{\mathbf{S}}\cdot\mathrm{d}\delta\mathbf{E} + \int_{\mathscr{B}}\delta\lambda\,(\mathrm{d}J - \mathrm{d}\theta)\\ &+ \int_{\mathscr{B}}\mathrm{d}\lambda(\delta J - \delta\theta) + \int_{\mathscr{B}}\lambda\,\mathrm{d}\delta J - \int_{\mathscr{B}}\mathrm{d}\mathbf{b}\cdot\delta\boldsymbol{\varphi} - \int_{\mathscr{S}^{\mathrm{u}}}\mathrm{d}\mathbf{t}\cdot\delta\boldsymbol{\varphi},\end{aligned} \tag{A.8}$$

where $\mathbf{R}$ are the equilibrium equations (16)–(18) (see (42) and (43) also). The first and second derivatives of J are

$$\begin{aligned}\delta J &= J\mathbf{C}^{-1}\cdot\delta\mathbf{E},\\ \mathrm{d}\delta J &= J(\mathbf{C}^{-1}\cdot\delta\mathbf{E})(\mathbf{C}^{-1}\cdot\mathrm{d}\mathbf{E}) - 2J(\mathbf{C}^{-1}\,\mathrm{d}\mathbf{E}\mathbf{C}^{-1})\cdot\delta\mathbf{E} + J\mathbf{C}^{-1}\cdot\mathrm{d}\delta\mathbf{E},\end{aligned} \tag{A.9}$$

since

$$\mathrm{d}\mathbf{C}^{-1} = -\mathbf{C}^{-1}\,\mathrm{d}\mathbf{C}\,\mathbf{C}^{-1}. \tag{A.10}$$

Using (A.9) in (A.8) we get

$$\begin{aligned}\mathrm{d}\mathbf{R} = &\int_{\mathscr{B}}\mathrm{d}\bar{\mathbf{S}}\cdot\delta\mathbf{E} + \int_{\mathscr{B}}(\bar{\mathbf{S}} + \lambda J\mathbf{C}^{-1})\cdot\mathrm{d}\delta\mathbf{E} + \int_{\mathscr{B}}\mathrm{d}\hat{\sigma}\delta\theta + \int_{\mathscr{B}}\left(\lambda J(\mathbf{C}^{-1}\cdot\mathrm{d}\mathbf{E})\mathbf{C}^{-1} - 2\lambda J(\mathbf{C}^{-1}\,\mathrm{d}\mathbf{E}\mathbf{C}^{-1})\right)\cdot\delta\mathbf{E}\\ &+ \int_{\mathscr{B}}(\mathrm{d}\lambda J\ \mathbf{C}^{-1}\cdot\delta\mathbf{E} + \delta\lambda\ J\mathbf{C}^{-1}\cdot\mathrm{d}\mathbf{E}) - \int_{\mathscr{B}}(\delta\lambda\,\mathrm{d}\theta + \mathrm{d}\lambda\ \delta\theta) - \int_{\mathscr{B}}\mathrm{d}\mathbf{b}\cdot\delta\boldsymbol{\varphi} - \int_{\mathscr{S}^{u}}\mathrm{d}\mathbf{t}\cdot\delta\boldsymbol{\varphi}.\end{aligned} \tag{A.11}$$

Second derivatives for the elastic stress $\bar{\mathbf{S}}_e$ are

$$\frac{\partial \bar{\mathbf{S}}_e}{\partial \mathbf{E}} = 4gf\left(\frac{\partial^2 \bar{\phi}}{\partial \bar{I}_1\,\partial \bar{I}_1}\left(\frac{\partial \bar{I}_1}{\partial \mathbf{C}} \otimes \frac{\partial \bar{I}_1}{\partial \mathbf{C}}\right) + \frac{\partial \bar{\phi}}{\partial \bar{I}_1}\frac{\partial^2 \bar{I}_1}{\partial \mathbf{C}\,\partial \mathbf{C}}\right), \tag{A.12}$$

where $\otimes$ is the standard tensor product and

$$\frac{\partial^2 \bar{\phi}}{\partial \bar{I}_1\,\partial \bar{I}_1} = 2\beta_2 + 6\beta_3(\bar{I}_1 - 3) + \beta_4\beta_5 e^{-\beta_5(\bar{I}_1 - 3)} \tag{A.13}$$

and

$$d\frac{\partial \bar{I}_1}{\partial \mathbf{C}} = -\frac{1}{3}\frac{\mathscr{I}}{I_3^{1/3}}(\mathbf{C}^{-1}\cdot d\mathbf{C}) - \frac{1}{3}\frac{(\mathscr{I}\cdot d\mathbf{C})}{I_3^{1/3}}\mathbf{C}^{-1} + \frac{1}{9}\frac{\mathscr{I}\cdot\mathbf{C}}{I_3^{1/3}}\mathbf{C}^{-1}(\mathbf{C}^{-1}\cdot d\mathbf{C}) + \frac{1}{3}\frac{\mathscr{I}\cdot\mathbf{C}}{I_3^{1/3}}\mathbf{C}^{-1}\,d\mathbf{C}\,\mathbf{C}^{-1}. \tag{A.14}$$

In components

$$\frac{\partial^2 \bar{I}_1}{\partial \mathbf{C}_{ij}\,\partial \mathbf{C}_{kl}} = -\frac{1}{3}\frac{\mathscr{I}_{ij}}{I_3^{1/3}}\mathbf{C}^{-1}_{kl} - \frac{1}{3}\frac{\mathscr{I}_{kl}}{I_3^{1/3}}\mathbf{C}^{-1}_{ij} + \frac{1}{9}\frac{\mathscr{I}\cdot\mathbf{C}}{I_3^{1/3}}\mathbf{C}^{-1}_{ij}\mathbf{C}^{-1}_{kl} + \frac{1}{3}\frac{\mathscr{I}\cdot\mathbf{C}}{I_3^{1/3}}\mathbf{C}^{-1}_{ik}\mathbf{C}^{-1}_{lj}. \tag{A.15}$$

The derivatives on the generalized viscoelastic stresses are obtained using (36) and noting that $d\mathbf{H}^i_n = 0$

$$d(\bar{\mathbf{S}}, \hat{\sigma})(t) = \left(G_\infty + \sum_{i=1}^{m}\frac{G_i}{\Delta t}\int_n^t e^{(\xi_\tau - \xi_t)/\tau_i}\,d\tau\right)d(\bar{\mathbf{S}}, \hat{\sigma})_e(t). \tag{A.16}$$

Second derivatives on $\hat{\sigma}_e$ are given by

$$\frac{\partial \hat{\sigma}_e}{\partial \theta} = \frac{K}{\theta_{th}^2\theta_c^2}. \tag{A.17}$$

References

[1] Ş. Özüpek, E.B. Becker, Constitutive equations for solid propellants, J. Engrg. Matls. Tech. 119 (1997) 125–132.
[2] J.C. Simo, On a fully three-dimensional finite-strain viscoelastic damage model: formulation and computational aspects, Comput. Methods Appl. Mech. Engrg. 60 (1987) 153–173.
[3] O.H. Yeoh, Some forms of the strain energy function for rubber, Rubber Chem. Technol. 66 (1993) 754–771.
[4] P.G. Ciarlet, Mathematical Elasticity, vol. I: Three-Dimensional Elasticity, North-Holland, Amsterdam, 1988.
[5] E.B. Becker, G.F. Carey, J.T. Oden, Finite Elements: An Introduction, vol. 1. Prentice-Hall, Englewood Cliffs, NJ, 1981.
[6] E.B. Becker, T. Miller, User's Manual for the TEXPAC Computer Code, Mechanics Software, Austin, Texas, 1989.
[7] J. Nelson, Linear viscoelastic characterization of redesigned solid rocket motor propellant, Interim Report TR-88-030, Thiokol Corporation, 1993.
[8] G.A. Collingwood, K.L. Laheru, M.D. Dixon, Minuteman III stage 1 motor service life estimate prediction through improved nonlinear viscoelastic techniques, Interim Engineering Report TR-10488, Thiokol Corporation, September 1995.